JACS
JOURNAL OF THE AMERICAN CHEMICAL SOCIETY
Article
pubs.acs.org/JACS

Codoping in SnTe: Enhancement of Thermoelectric Performance through Synergy of Resonance Levels and Band Convergence

Gangjian Tan,[†] Fengyuan Shi,[‡] Shiqiang Hao,[‡] Hang Chi,[§] Li-Dong Zhao,[†] Ctirad Uher,[§] Chris Wolverton,[‡] Vinayak P. Dravid,[‡] and Mercouri G. Kanatzidis*[,†,∥]

[†]Department of Chemistry and [‡]Department of Materials Science and Engineering, Northwestern University, Evanston, Illinois 60208, United States

[§]Department of Physics, University of Michigan, Ann Arbor, Michigan 48109, United States

[∥]Materials Science Division, Argonne National Laboratory, Argonne, Illinois 60439, United States

Supporting Information

ABSTRACT: We report a significant enhancement of the thermoelectric performance of p-type SnTe over a broad temperature plateau with a peak ZT value of ~1.4 at 923 K through In/Cd codoping and a CdS nanostructuring approach. Indium and cadmium play different but complementary roles in modifying the valence band structure of SnTe. Specifically, In-doping introduces resonant levels inside the valence bands, leading to a considerably improved Seebeck coefficient at low temperature. Cd-doping, however, increases the Seebeck coefficient of SnTe remarkably in the mid- to high-temperature region via a convergence of the light and heavy hole bands and an enlargement of the band gap. Combining the two dopants in SnTe yields enhanced Seebeck coefficient and power factor over a wide temperature range due to the synergy of resonance levels and valence band convergence, as demonstrated by the Pisarenko plot and supported by first-principles band structure calculations. Moreover, these codoped samples can be hierarchically structured on all scales (atomic point defects by doping, nanoscale precipitations by CdS nanostructuring, and mesoscale grains by SPS treatment) to achieve highly effective phonon scattering leading to strongly reduced thermal conductivities. In addition to the high maximum ZT the resultant large average ZT of ~0.8 between 300 and 923 K makes SnTe an attractive p-type material for high-temperature thermoelectric power generation.

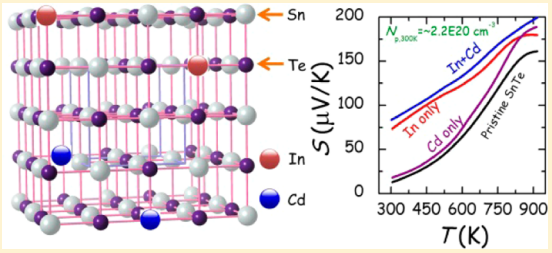

INTRODUCTION

Thermoelectrics can realize the direct conversion of heat to electric power in the absence of any moving parts or liquid media.[1] This solid-state and highly reliable technology has a long history of powering the spacecrafts of NASA deep-space missions[2] and is now being actively developed for use in waste heat recovery.[3−5] The conversion efficiency of thermoelectric technology is closely related to the dimensionless figure of merit (ZT) expressed as $ZT = S^2\sigma T/(\kappa_{elc} + \kappa_{lat})$. In this expression, S is the Seebeck coefficient, σ is the electrical conductivity, T is the absolute temperature, and κ_{elc} and κ_{lat} represent the electrical and lattice contribution to the total thermal conductivity ($\kappa_{tot} = \kappa_{elc} + \kappa_{lat}$), respectively. As these parameters are subtly interrelated, one needs to carefully tailor them to optimize the final ZTs.

Lead chalcogenides and their solid solutions (PbQ, Q = S, Se, and Te) have long been recognized as high-temperature thermoelectric materials with outstanding performance.[6−12] Using the concepts of band engineering (resonant levels,[13−17] band convergence,[18−22] bands alignment,[23−25] etc.) and microstructure manipulation on all scales,[8,10,23,26−31] the highest ZT of PbTe has steadily climbed to over 2.[22,26,31] These strategies have recently been applied to tin chalcogenides (SnQ)[17,32−37] which are perceived to be more environmentally friendly than PbQ, with the goal to improve their performance to the same level as PbTe. Among SnQ, only SnTe adopts the same rock salt structure as PbQ and is an ideal candidate to test whether these ideas for enhancing ZT still work for SnQ. It should be noted here that a record high ZT of 2.6 has been reported recently in SnSe single crystal[38] which is a non-rocksalt layered material exhibiting an exceptionally low thermal conductivity due to highly anharmonic bonding.

Similar to PbQ, SnTe has a two-valence band structure.[39,40] The difference is that the room-temperature energy separation (ΔE) between the so-called upper light-hole band at L point and lower heavy-hole band at Σ point of SnTe (~0.3−0.4 eV)[39,40] is much larger than in PbTe (for example, ΔE ~0.17 eV[41,42]). This larger ΔE in SnTe means that the heavy-hole band contributes little to the Seebeck coefficient. Indeed, in pure SnTe, the room-temperature Seebeck coefficient is very low <40 μV/K, depending on the hole concentration.[33,39,43]

Bushmarina[44] et al. and Zhang et al.[17] reported that the introduction of indium in SnTe could create resonant levels

Received: January 25, 2015
Published: April 9, 2015

DOI: 10.1021/jacs.5b00837
J. Am. Chem. Soc. 2015, 137, 5100−5112

inside the valence band. This enhances the Seebeck coefficient around room temperature, while with increasing temperature, the enhancement diminishes.[17] This is similar to the Tl-doped PbTe system which enhances its Seebeck coefficient at room temperature and below, but the effect weakens significantly above 500 K.[13,14] This confirms previous conclusions that resonant levels usually work at relatively low temperatures and are not useful in enhancing ZT at high temperatures.[1,14,45]

In our previous study,[32] we demonstrated that cadmium modifies the band structure of SnTe in two ways: (i) it significantly lowers ΔE, which results in increased hole density of states and enhanced Seebeck coefficients, especially in the high-temperature range; and (ii) it enlarges the band gap, which minimizes the minority carriers at elevated temperature, and inhibits bipolar conduction. These results indicate that indium and cadmium have distinct but complementary roles, and if they were to be present at the same time (codoping) in SnTe, they could produce enhanced Seebeck coefficients and ZTs over a broad temperature range. This ZT enhancement over a wide temperature range has not been found in previous studies of SnTe, but it is highly desirable for practical applications, where the efficiency of a thermoelectric device is directly determined by its average ZT (ZT_{ave}) not the maximum ZT (ZT_{max}).[2]

In this contribution we report results that demonstrate the coexistence of resonant levels induced by indium doping and band convergence enabled by cadmium doping in p-type SnTe. This type of codoping, produces a significant enhancement of the Seebeck coefficient and ZT over a broad temperature range (300−950 K) compared to any other reported optimized SnTe material. Namely, the obtained performance is superior to (i) the undoped SnTe material, (ii) SnTe optimally doped with indium, and (iii) SnTe optimally doped with Cd. Moreover, we demonstrate a strong reduction in the thermal conductivity of codoped SnTe by employing nanoscaled CdS precipitates coupled with mesoscale grains (introduced by spark plasma sintering treatment) to form all-scale hierarchical microstructures. As a consequence, the ZT can reach the maximum value of ∼1.4 at 923 K. Notably, a ZT_{ave} of ∼0.8 between 300 and 923 K was achieved in 1.5% In and 1.5% Cd codoped SnTe nanostructured with 3% CdS compared to ∼0.47 in SnTe doped with In and ∼0.42 doped with Cd. This is the highest value achieved to date making SnTe a robust candidate for high-temperature thermoelectric power generation when lead-free materials are desired.

EXPERIMENTAL SECTION

Synthesis. Reagent chemicals were used as obtained: Sn chunk (99.9999%, American Elements, US), In ingot (99.99%, American Elements, US), Cd shot (99.99%, Alfa, US), Te shot (99.999%, 5N Plus, Canada), and S chunk (99.999%, 5N Plus, Canada).

Weighing. High-purity single elements Sn, In, Cd, Te, and S were weighed according to the nominal compositions of $Sn_{1-x}In_xTe$ (x = 0, 0.005, 0.01, 0.015, 0.02), $Sn_{1-x}Cd_xTe$ (x = 0.005, 0.01, 0.015, 0.02), $Sn_{1-x}In_{x/2}Cd_{x/2}Te$ (x = 0.005, 0.01, 0.015, 0.02, 0.03, 0.04), and $Sn_{0.97}In_{0.015}Cd_{0.015}Te$-$x$%CdS ($x$ = 1, 2, 3, 4, and 5, in mole ratio) and then put inside 13 mm diameter fused quartz tubes. The tubes were then evacuated to a residual pressure of ∼10^{-4} Torr and flame-sealed. For a typical experiment the following amounts were used: Sn (3.6775 g, 30.98 mmol), In (0.0550 g, 0.4791 mmol), Cd (0.1616 g, 1.437 mmol), Te (4.0752 g, 31.9372 mmol), and S (0.0307 g, 0.958 mmol) were used to prepare 8 g of $Sn_{0.97}In_{0.015}Cd_{0.015}Te$-3%CdS.

Melting. The loaded tubes were melted in computer controlled furnaces. For compositions without CdS, the samples were slowly heated to 1273 K in 10 h, soaked at this temperature for 8 h, then slowly cooled to 1073 K in 2 h, dwelled at this temperature for another 3 h, and subsequently cooled to room temperature by turning off the furnace power. For compositions containing CdS, the samples were slowly heated to 723 K in 10 h, soaked at this temperature for 6 h, then to 1423 K in 7 h, soaked at this temperature for 10 h, and subsequently quenched in water. The tubes were periodically shaken during the melting process to promote the complete reaction among elements and ensure the homogeneity of the compositions.

Densification. The resultant ingots were crushed into fine powders and then densified by spark plasma sintering (SPS) method (SPS-211LX, Fuji Electronic Industrial Co., Ltd.) at 773 K for 5 min in a 12.7 mm diameter graphite die under an axial compressive stress of 40 MPa in vacuum. Highly dense (>96% of theoretical density, Table S1) disk-shaped pellets with dimensions of 12.7 mm in diameter and 8 mm in thickness were obtained.

Electron Microscopy and X-ray Diffraction. (Scanning) transmission electron microscopy ((S)TEM) and STEM energy dispersive spectroscopy (EDS) experiments investigations were carried out using a JEOL 2100F microscope operated at 200 kV. The thin TEM specimens were prepared by conventional methods, including cutting, grinding, dimpling, tripod, with minimal duration of Ar-ion milling with a liquid N_2 cooling stage. Samples pulverized with an agate mortar were used for powder X-ray diffraction (XRD). The powder diffraction patterns were obtained with Cu K_α (λ = 1.5418 Å) radiation in a reflection geometry on an Inel diffractometer operating at 40 kV and 20 mA and equipped with a position-sensitive detector. All samples investigated in this study are practically single phase compounds (at the limit of our XRD instrument) with rock salt structure and no detectable second phases, Figure S1.

Physical Characterization. *Electrical Properties.* The obtained SPS processed pellets were cut into bars with dimensions 12 × 3 × 3 mm^3 for simultaneous measurement of the Seebeck coefficient and electrical conductivity using an Ulvac Riko ZEM-3 instrument under a low-pressure helium atmosphere from room temperature to 923 K. The uncertainties of the Seebeck coefficient and electrical conductivity measurements are ∼5% and 10%, respectively.[46]

Thermal Conductivity. Highly dense SPS processed pellets were cut and polished into a squared shape of 6 × 6 × 2 mm^3 for thermal diffusivity measurements. The samples were coated with a thin layer of graphite to minimize errors from the emissivity of the material. The thermal conductivity was calculated from $\kappa = D \cdot C_p \cdot d$, where the thermal diffusivity coefficient (D) was measured using the laser flash diffusivity method in a Netzsch LFA457, the specific heat capacity (C_p) was indirectly derived using a reference sample (Pyroceram 9606) in the range 300−923 K, and the density (d) was determined using the dimensions and mass of the sample. The thermal diffusivity data were analyzed using a Cowan model with pulse correction. The measured densities of all the samples range between 6.2 and 6.3 g·cm^{-3} or are above 96% of the theoretical densities, Table S1. The uncertainty of the thermal conductivity is estimated to be within 16%, considering all the uncertainties from D (∼5%), C_p (∼15%), and d.[46] The heat capacity and the thermal diffusion data for all samples can be found in Figures S2 and S3, respectively. The combined uncertainty for all measurements involved in the calculation of ZT is around 20%. Unless otherwise noted, all the properties described in this study were measured perpendicular to the sintering pressure direction, although no directional anisotropy effects were observed in the charge transport properties.

Hall Measurements. The room-temperature Hall measurement was performed on a homemade apparatus (University of Michigan). The Hall resistance was monitored with a Linear Research AC Resistance Bridge (LR-700), with constant magnetic fields of ±1 T applied by using an Oxford superconducting magnet. The effective carrier concentration (N_p) was estimated using the relationship $N_p = 1/eR_H$, where e is the elemental charge, and R_H is the Hall coefficient. The Hall mobility (μ_H) was calculated using the relationship $\mu_H = \sigma R_H$ with σ being the electrical conductivity obtained from ZEM-3 instrument.

DOI: 10.1021/jacs.5b00837
J. Am. Chem. Soc. 2015, 137, 5100−5112

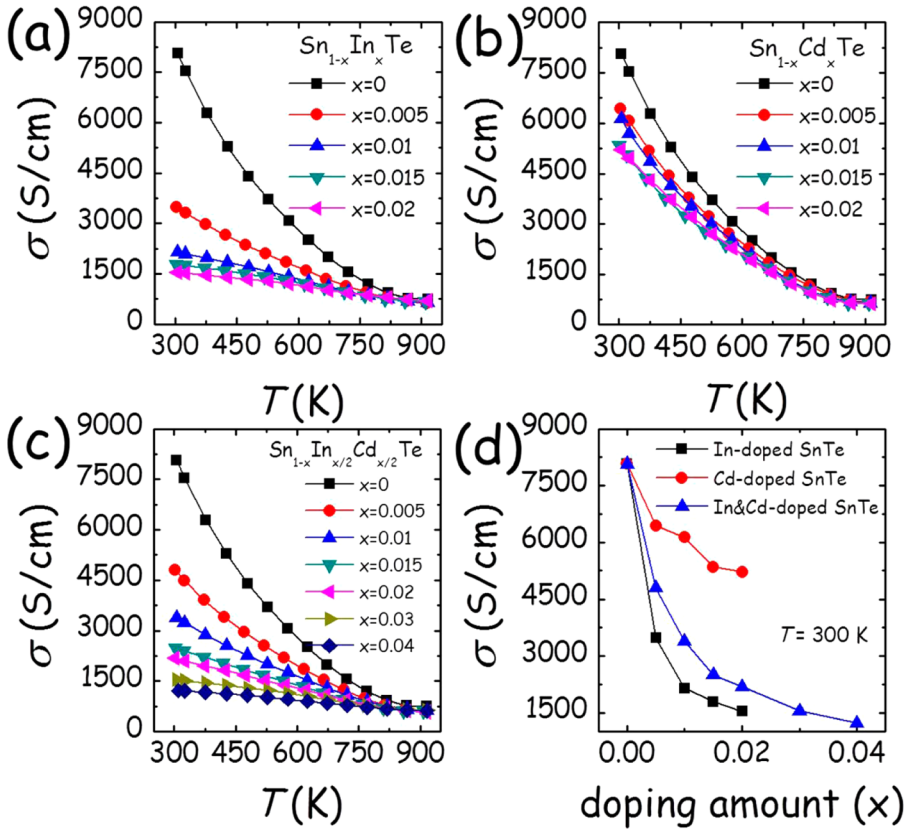

Figure 1. Electrical conductivities (σ) as a function of temperature for (a) $Sn_{1-x}In_xTe$, (b) $Sn_{1-x}Cd_xTe$, and (c) $Sn_{1-x}In_{x/2}Cd_{x/2}Te$. (d) Room temperature σ as a function of doping amount (x) for all the samples.

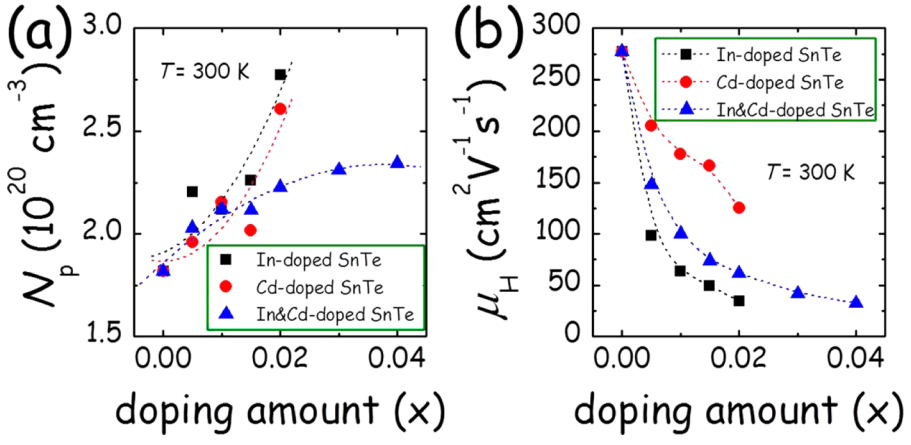

Figure 2. Room-temperature (a) carrier concentrations (N_p) and (b) mobilities (μ_H) as a function of doping amount (x) for $Sn_{1-x}In_xTe$, $Sn_{1-x}Cd_xTe$, and $Sn_{1-x}In_{x/2}Cd_{x/2}Te$. The lines are guide to eyes.

Band Structure Calculations. Density functional theory (DFT) calculations of pristine, stoichiometric SnTe, Cd- and In-doped, and Cd and In codoped SnTe were carried out. The calculations were performed using the generalized gradient approximation with PBE[47] functional for the exchange−correlation functional and projector augmented wave potentials as implemented in Vienna Ab initio Simulation Package (VASP).[48] All structures are fully relaxed with respect to cell vectors and cell-internal positions. The electronic density of states (DOS) is calculated from the relaxed structures using the tetrahedron method with Blöchl corrections. For the Sn and In species, the 5d electrons are treated as valence states. The total energies were numerically converged to approximately 3 meV/cation using a basis set energy cutoff of 400 eV and dense k-meshes corresponding to 4000 k-points per reciprocal atom in the Brillouin zone.

To investigate the movements of the conduction band and valence bands (L and Σ bands), we considered 3 × 3 × 3 supercells of NaCl-type $Sn_{27}Te_{27}$. For the isovalent doping of Cd, we consider a single Cd impurity (~3.7% additions of Cd, $Sn_{26}Cd_1Te_{27}$) with Cd substituting for Sn. For the aliovalent In dopant, we consider a range of defect types: In interstitials (In_i^{3+}), In substitution (In_{Sn}^{+}), Te vacancy (V_{Te}^{2-}), and multiple defect complexes ($2In_{Sn}^{+} + V_{Te}^{2-}$) to identify the most favorable In-related defect configuration in SnTe. The calculation results show that the most favorable defect is In substitution of Sn (In_{Sn}^{+}), which is about 1.7 eV more favorable than the neutral defect complex ($2In_{Sn}^{+} + V_{Te}^{2-}$). For the case of In and Cd codoping, we find that first and second nearest-neighbor (In + Cd) configurations have

DOI: 10.1021/jacs.5b00837
J. Am. Chem. Soc. 2015, 137, 5100−5112

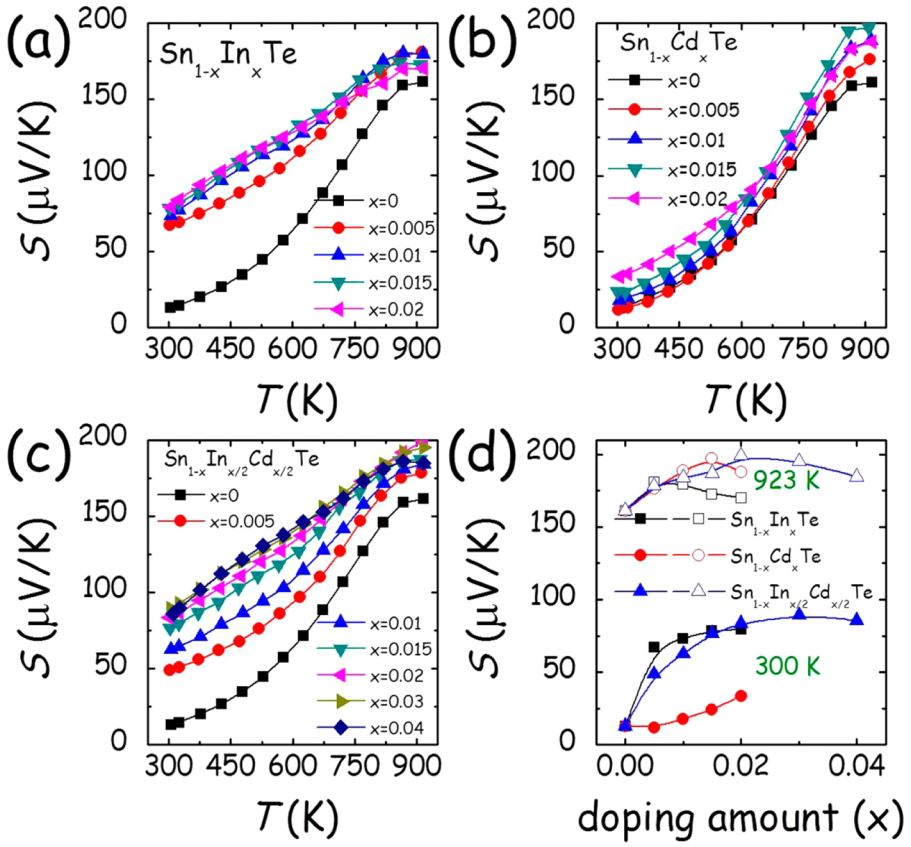

Figure 3. Temperature-dependent Seebeck coefficients (S) for (a) $Sn_{1-x}In_xTe$, (b) $Sn_{1-x}Cd_xTe$, and (c) $Sn_{1-x}In_{x/2}Cd_{x/2}Te$. (d) 300 and 923 K Seebeck coefficients as a function of doping amount (x) for SnTe with different dopants.

formation energies which are unfavorable relative to the isolated impurities. We calculated Cd−In defect pairs in the third nearest-neighbor positions on the Sn sublattice. The substitution defects in SnTe completely change the symmetry of the original primitive cell. Thus, for the purposes of a more direct comparison with SnTe we transformed the eigenstates for defect structures into a so-called effective band structure in the primitive Brillouin zone of the parent compound SnTe using a spectral decomposition method.[49,50] Using this approach, we are able to calculate the energy level of the L-point and Σ-line and the corresponding energy differences for the supercells with defects.

RESULTS AND DISCUSSION

Electrical Transport Properties of Doped SnTe. In order to better assess the effects of codoping of In and Cd in the SnTe structure, we also prepared single doped $Sn_{1-x}In_xTe$ and $Sn_{1-x}Cd_xTe$ samples for comparison. Figures 1(a), (b) and (c) show the temperature-dependent electrical conductivities for $Sn_{1-x}In_xTe$, $Sn_{1-x}Cd_xTe$ and $Sn_{1-x}In_{x/2}Cd_{x/2}Te$, respectively. Clearly, for all samples, the electrical conductivity decreases steadily with increasing temperature up to 923 K, typical of metallic conduction and a heavily doped state. Figure 1d summarizes the room-temperature electrical conductivities as a function of doping concentration for all the samples. In all cases, the electrical conductivity decreases with increasing amount of dopant. However, one can see that with identical doping amount, the singly In-doped samples have much lower electrical conductivities than singly Cd-doped samples, while the In and Cd codoped samples have intermediate values.

Hall measurements were carried out at room temperature to estimate the carrier concentration with different dopant types and content. The resultant carrier concentration N_p and mobility μ_H are plotted in Figure 2a,b, respectively. N_p is positive for all samples, showing p-type conduction. Pristine SnTe has a high hole concentration of ~1.8 × 10^{20} cm^{-3} at room temperature because of the existence of intrinsic Sn vacancies.[51] In all cases, the room-temperature N_p roughly increases with increasing doping amount, which, however, is contradictory to the expected electron donor role of In in SnTe and is also inconsistent with our previous findings[32] that Cd serves as an efficient hole neutralizer in Sn self-compensated SnTe. As pointed out above, SnTe is a typical non-stoichiometric compound with inherent Sn vacancies.[51,52] Each Sn vacancy acts as a two-electron acceptor. When In is doped into SnTe, it will preferentially occupy Sn vacancies and thus becomes an one-electron acceptor which increases the hole densities accordingly.[17] Similarly, the role played by Cd here is different as it tailors the carrier concentrations of Sn-compensated SnTe.[32] The high hole densities found in these samples also support their metal-like electrical conductivities.

Pristine SnTe has a high hole mobility of ~280 cm^2 V^{-1} s^{-1} at 300 K, which together with its high hole density produces a large electrical conductivity of ~8070 S/cm at room temperature. Upon doping with In or/and Cd, μ_H decreases significantly and leads to the decline of the electrical conductivity described above. With increasing the doping amount of In or/and Cd, μ_H is systematically decreased, presumably because of the enhanced point defect scattering, increased scattering between carriers, and, as we will discuss later, higher effective mass of holes in In or/and Cd-doped SnTe relative to pristine SnTe caused by band structure

DOI: 10.1021/jacs.5b00837
J. Am. Chem. Soc. 2015, 137, 5100−5112

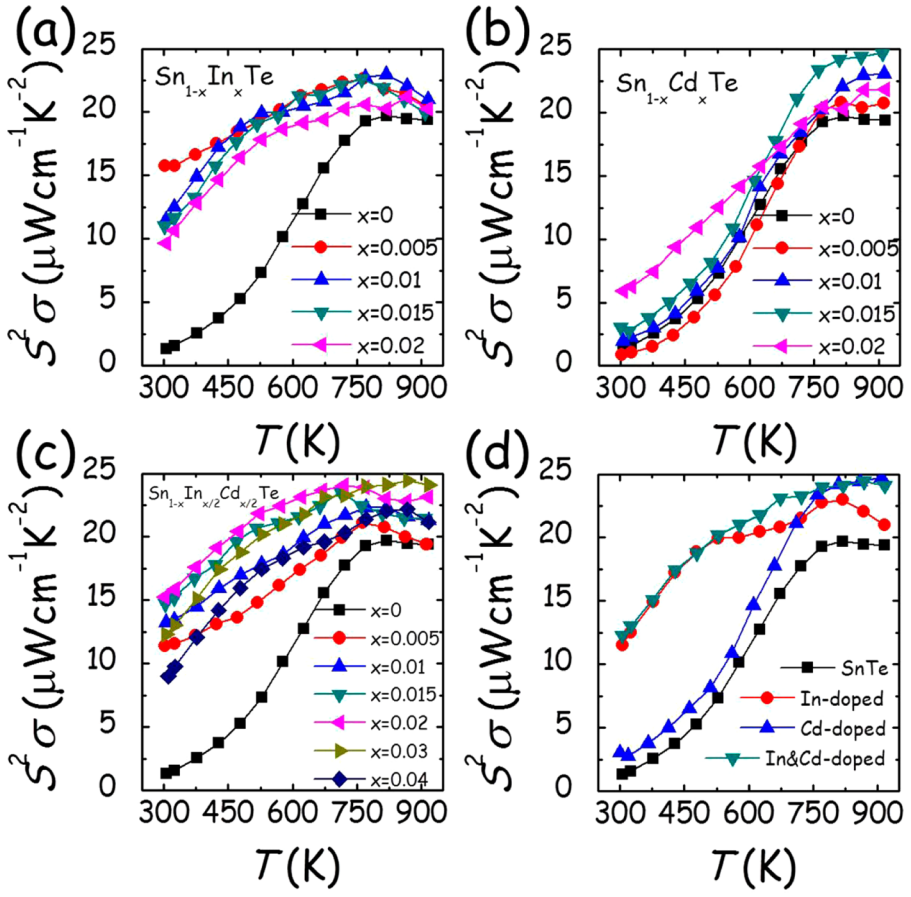

Figure 4. Power factors as a function of temperature for (a) $Sn_{1-x}In_xTe$, (b) $Sn_{1-x}Cd_xTe$, and (c) $Sn_{1-x}In_{x/2}Cd_{x/2}Te$. (d) Comparison of power factors between pristine SnTe and doped SnTe with optimized compositions.

modification. On the other hand, with identical doping concentrations, Cd-doped SnTe samples have the highest hole mobilities, while In-doped samples have the lowest. In and Cd codoped samples always have intermediate values, similar to the trend observed in the electrical conductivities. This suggests that the high electrical conductivities in these materials are mainly due to the high carrier mobilities. The difference of μ_H in samples with different dopant concentration and dopant type may originate partly from their different N_p and partly from the different effective mass of holes caused by the difference in the valence band structures, as will be discussed later.

The Seebeck coefficients as a function of temperature for $Sn_{1-x}In_xTe$, $Sn_{1-x}Cd_xTe$, and codoped $Sn_{1-x}In_{x/2}Cd_{x/2}Te$ are shown in Figure 3a–c, respectively. All Seebeck coefficients are positive and consistent with the signs of the Hall carrier concentrations. As can be seen from Figure 3a, the room-temperature Seebeck coefficient of $Sn_{1-x}In_xTe$ (x = 0.005) is notably enhanced relative to pristine SnTe from ~13 to ~67 μV/K, a 400% improvement. However, with increasing temperature, the magnitude of the enhancement diminishes. Specifically, at 923 K, the Seebeck coefficients of pristine and In-doped SnTe are ~161 and 170–180 μV/K, respectively. On the contrary, for the Cd-doped SnTe, the Seebeck enhancement is small near room temperature, but it gets more pronounced in the high-temperature range with the highest values reaching ~200 μV/K at 923 K, Figure 3b. Interestingly, when combining the In and Cd dopants together, Figure 3c, the Seebeck coefficients are dramatically increased relative to pristine SnTe over the whole temperature range. For example, the Seebeck coefficients of $Sn_{0.97}In_{0.015}Cd_{0.015}Te$ at 300 and 923 K are ~84 and 199 μV/K, respectively. Figure 3d compares the 300 and 923 K Seebeck coefficients of SnTe with different dopants. One can see that under same doping level, at 300 K, the Seebeck coefficients of In and Cd codoped SnTe are closer to those of In-doped (much higher than in the Cd singly doped case), while at 923 K, they are closer to those of Cd-doped SnTe (higher than the In singly doped case), and this trend becomes more obvious at a higher x. This demonstrates that In and Cd codoping in SnTe is synergic and combines the merits of In and Cd single doping, contributing to the Seebeck coefficient enhancement of SnTe over a very wide temperature range.

The temperature-dependent power factors ($S^2\sigma$) as a function of temperature for $Sn_{1-x}In_xTe$, $Sn_{1-x}Cd_xTe$, and $Sn_{1-x}In_{x/2}Cd_{x/2}Te$ are shown in Figure 4a–c, respectively. Because of the increased Seebeck coefficients upon doping, the power factors are enhanced as well relative to pristine SnTe. For In-doped SnTe, the power factor enhancement is especially noticeable below 800 K, while for the Cd-doped samples, the enhancement is realized above 700 K. In and Cd codoping of SnTe enables a remarkable increase of power factors over the entire temperature range. Figure 4d compares the optimized power factors for pristine, In- and Cd-doped, and In and Cd codoped SnTe. Clearly, In and Cd codoped SnTe combines the merits of solely In doping and solely Cd doping. Specifically, in comparison with pristine SnTe, it has greatly increased power factors both at low temperature (below 800 K, similar to In-doped SnTe) and at high temperature (>700 K, analogous to

DOI: 10.1021/jacs.5b00837
J. Am. Chem. Soc. 2015, 137, 5100–5112

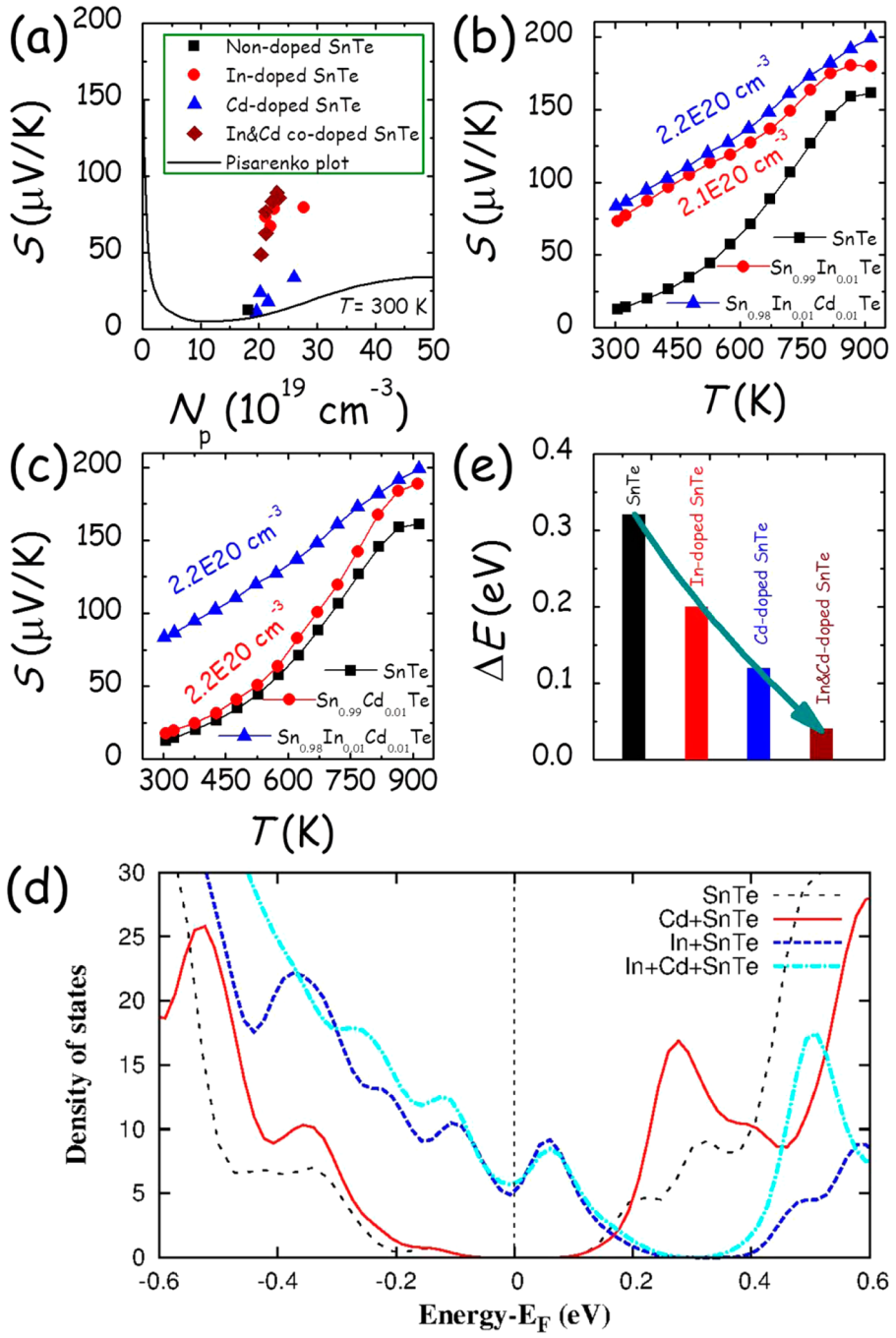

Figure 5. (a) Room-temperature Seebeck coefficients (S) as a function of carrier concentrations (N_p) for SnTe with different dopants. The solid line is Pisarenko plot calculated using a two-valence-band model.[17] A comparison of temperature-dependent Seebeck coefficients for (b) SnTe, $Sn_{0.99}In_{0.01}Te$ and $Sn_{0.98}In_{0.01}Cd_{0.01}Te$ and (c) SnTe, $Sn_{0.99}Cd_{0.01}Te$ and $Sn_{0.98}In_{0.01}Cd_{0.01}Te$. (d) DOS near the top valence band and (e) energy separations ΔE between the upper valence band at L point and the lower valence band at Σ point for pristine SnTe, In- and Cd-doped SnTe, and In and Cd codoped SnTe.

Cd-doped SnTe). This indicates an additive and possibly synergistic effect in codoped samples.

Band Structure Modifications with Different Dopants in SnTe. To understand the origin of Seebeck coefficient enhancement in doped SnTe, we compare the room-temperature S–N_p plot with the well-established Pisarenko line which is calculated based on a two-valence-band model,[17] Figure 5a. The data point for pristine SnTe falls exactly on the Pisarenko line, demonstrating the validity of the adopted physical model.[17] The In-doped SnTe samples, however, have much higher Seebeck coefficients than predicted by the Pisarenko relation, which was reported to arise from the resonant levels inside the valence band introduced by the In dopant.[17,44] This doping sharply increases the effective mass of holes (and therefore significantly decreases the hole mobilities, Figure 2b). The Cd-doped SnTe samples also have larger than predicted Seebeck coefficients, but this enhancement is more evident in the samples with higher Cd content (i.e., higher hole concentrations). In our previous study[32] we reported that the introduction of Cd in SnTe can decrease the energy separation

DOI: 10.1021/jacs.5b00837
J. Am. Chem. Soc. 2015, 137, 5100–5112

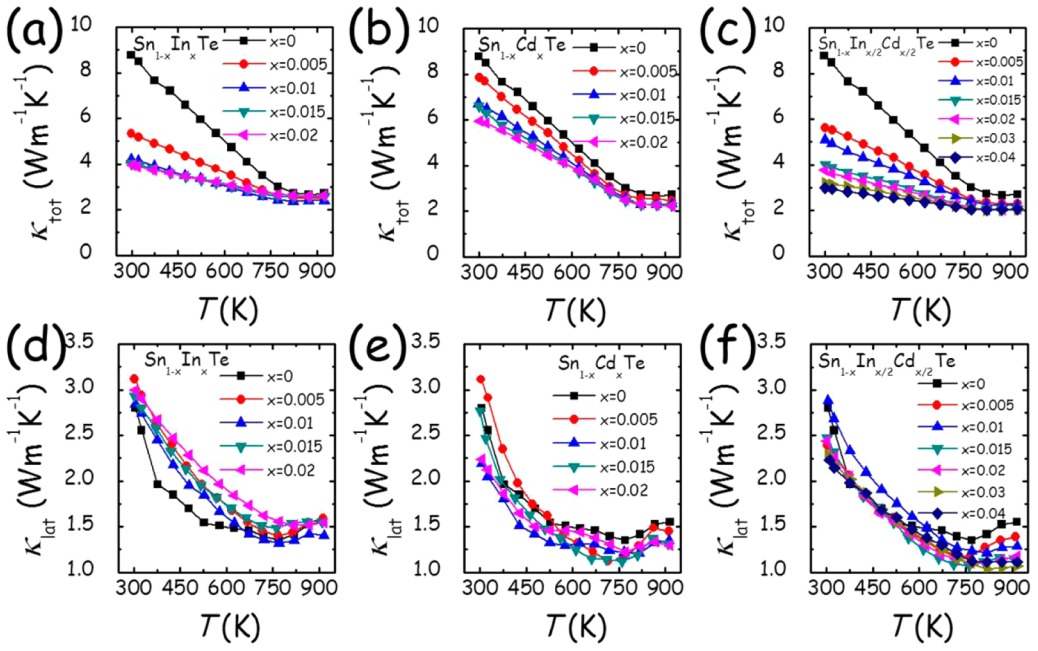

Figure 6. (a–c) Total (κ_{tot}) and (d–f) lattice thermal conductivities (κ_{lat}) as a function of temperature for $Sn_{1-x}In_xTe$, $Sn_{1-x}Cd_xTe$, and $Sn_{1-x}In_{x/2}Cd_{x/2}Te$, respectively.

between the two valence bands, leading to band convergence, and this effect is proportional to the Cd content. Therefore, in higher Cd content samples, better band convergence is obtained between the light and the heavy hole bands that leads to enhanced Seebeck coefficients. As compared to resonant levels which strongly scatter carriers, the influence of band convergence on carrier mobility is much smaller. This is the reason why no significant loss of hole mobility is seen in the Cd-doped SnTe, Figure 2b.

We also find that In and Cd codoped SnTe have significantly higher Seebeck coefficients at room temperature than predicted by the Pisarenko plot, which is very similar to In-doped SnTe. Moreover, these In and Cd codoped samples have large Seebeck coefficients at high temperature (~200 μV/K) that are very close to those of Cd-doped ones, Figure 3c. These indicate that resonant levels introduced by the In dopant and band convergence caused by the Cd dopant may synergistically and harmoniously coexist in In and Cd codoped SnTe. While it is challenging to differentiate the two effects experimentally, we can qualitatively demonstrate their presence by comparing the temperature-dependent Seebeck coefficients of $Sn_{0.99}In_{0.01}Te$, $Sn_{0.99}Cd_{0.01}Te$ and $Sn_{0.98}In_{0.01}Cd_{0.01}Te$ with comparable hole concentrations (N_p are 2.1 × 10^{20}, 2.2 × 10^{20}, and 2.2 × 10^{20} cm^{-3}, respectively, for the three samples at room temperature), Figure 5b,c. If Cd is only a charge carrier regulator (pure dopant) in In and Cd codoped SnTe, then $Sn_{0.99}In_{0.01}Te$ and $Sn_{0.98}In_{0.01}Cd_{0.01}Te$ should have the same Seebeck coefficients. However, this is not the case experimentally as shown in Figure 5b. The codoped sample always has a higher Seebeck coefficient than the In-doped sample in the entire temperature range with large difference at T > 800 K. The larger difference is believed to arise from the band convergence effect which is more pronounced at high temperatures. This indicates that Cd cannot be viewed as a pure dopant in In- and Cd-doped SnTe and enhances the Seebeck coefficient by modifying the band structure, i.e., valence band convergence. Likewise, if In has no effect on the band structure of In and Cd codoped SnTe, $Sn_{0.99}Cd_{0.01}Te$ and $Sn_{0.98}In_{0.01}Cd_{0.01}Te$ should have similar Seebeck coefficients, which, however, is contrary to the experimental findings, Figure 5c. This means that In does not serve as a simple dopant in In and Cd codoped SnTe either. The positive influence In has on the Seebeck coefficient is presumably by introducing resonant levels in the valence bands as it does in pure SnTe.[17,44]

The coexistence of resonant levels and valence band convergence in In and Cd codoped SnTe is further supported by first-principles DFT calculations. Figure 5d displays the respective DOS near the top of the valence band of pristine SnTe, In-doped SnTe, Cd-doped SnTe, and In and Cd codoped SnTe. The DOS plots show well-defined peaks near the Fermi level inside the valence bands of both In-doped SnTe and In and Cd codoped SnTe. These peaks, however, are absent in pristine SnTe and Cd-doped SnTe. These results indicate that the resonant levels described above are associated only with the In dopant and are still present when incorporating Cd atoms in the lattice.

The calculated electronic band structures are shown in Figure S4. Figure 5e plots the energy separations ΔE between the two valence bands for all cases. It can be clearly seen that pure SnTe has a large ΔE of ~0.32 eV, while it decreases markedly to only 0.12 eV upon Cd-doping, consistent with our previous report.[32] Interestingly, one can find a similar but weaker reduction of ΔE in In-doped SnTe (0.20 eV), which has not been reported before. In and Cd codoping yields an even lower ΔE of 0.04 eV. It can therefore be concluded that band convergence still exists and plays a significant role in In and Cd codoped SnTe. Therefore, the coexistence of resonant levels and band convergence in the SnTe produce the observed Seebeck coefficient enhancement over the wide temperature range of 300–900 K.

Thermal Transport Properties and *ZT* Values of Doped SnTe. Figure 6a–c displays the total thermal conductivities κ_{tot} as a function of temperature for $Sn_{1-x}In_xTe$, $Sn_{1-x}Cd_xTe$, and $Sn_{1-x}In_{x/2}Cd_{x/2}Te$, respectively. They show a

DOI: 10.1021/jacs.5b00837
J. Am. Chem. Soc. 2015, 137, 5100–5112

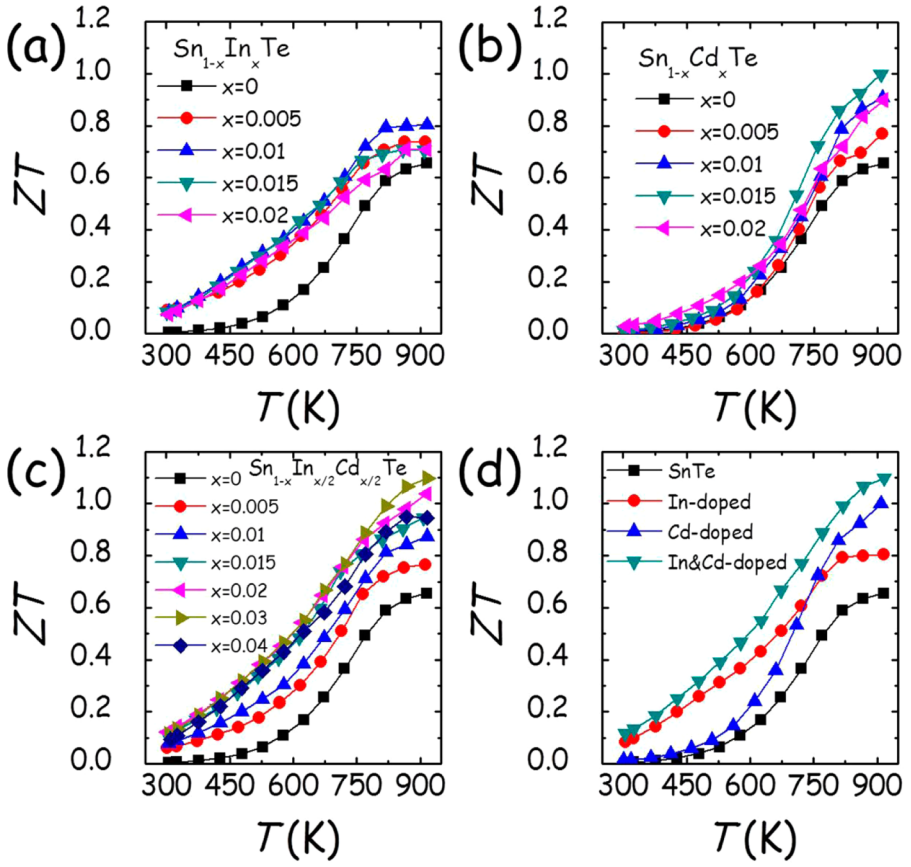

Figure 7. Temperature-dependent *ZT* values for (a) $Sn_{1-x}In_xTe$, (b) $Sn_{1-x}Cd_xTe$, and (c) $Sn_{1-x}In_{x/2}Cd_{x/2}Te$. (d) Comparison of *ZT*s between pristine SnTe and doped SnTe with optimized compositions.

significant decrease trend with increasing doping concentration in all cases. κ_{tot} is a sum of electrical (κ_{ele}) and lattice thermal conductivity (κ_{lat}). κ_{ele} is proportional to the electrical conductivity (σ) according to the Wiedemann–Franz relation $\kappa_{ele} = L\sigma T$ with L being the Lorenz number. In this study, L was obtained from the broadly adopted approach of fitting the Seebeck coefficient to the reduced chemical potential,[26,53,54] Figure S5. The temperature-dependent κ_{lat} for all samples is plotted in Figure 6d–f, respectively, and shows no specific trends with doping concentration or dopant type. Point defect scattering introduced by doping helps to reduce the κ_{lat} of SnTe, but the reduction is moderate because of the small atomic mass and size differences between the host atoms (Sn) and dopants (In and Cd). It is also worth noting that our In-doped SnTe shows higher κ_{lat} (and lower *ZT* shown below) in comparison with the values obtained in an earlier report where stronger phonon scattering was achieved via grain boundary refinement using a ball milling approach.[17] The lowest κ_{lat} of our coarse-grained samples in this study is still higher than 1 Wm^{-1} K^{-1} which is much larger than the theoretical minimum lattice thermal conductivity (κ_{min} = ~0.5 Wm^{-1} K^{-1})[36,55] for the SnTe-based material calculated using the Cahill model.[56] It suggests that there is still significant room to decrease κ_{lat} through combining other ways, for example, nanostructuring.[57,58]

The temperature-dependent *ZT* values for $Sn_{1-x}In_xTe$, $Sn_{1-x}Cd_xTe$, and $Sn_{1-x}In_{x/2}Cd_{x/2}Te$ are shown in Figures 7a–c, respectively. In-doping significantly increases *ZT*s of SnTe in the low-temperature range, while at elevated temperature the enhancement is marginal. Cd-doping, on the other hand, cannot increase the low-temperature *ZT* of SnTe, but with increasing temperature the *ZT*s of Cd-doped SnTe increase rapidly and surpass those of pristine SnTe by a large margin.

The In and Cd codoped SnTe combines the merits of In-doping and Cd-doping, i.e., the *ZT* values are enhanced over the whole temperature range. The maximum *ZT*s for pristine SnTe, $Sn_{1-x}In_xTe$, $Sn_{1-x}Cd_xTe$, and $Sn_{1-x}In_{x/2}Cd_{x/2}Te$ are 0.65, 0.80, 1.00, and 1.10 at ~923 K, respectively, Figure 7d. The improved *ZT*s over the broad range 300–900 K found in the codoped SnTe make it a useful thermoelectric material that deserves further investigation and performance optimization especially in view of their still high κ_{lat}. In the next section, we show how to increase the performance of $Sn_{0.97}In_{0.015}Cd_{0.015}Te$ by a nanostructuring approach.

Nanostructuring of In/Cd Codoped SnTe with CdS. We selected CdS as the second phase to increase the thermal resistance because it has shown rather limited solubility and well-behaved nucleation and growth in SnTe.[32] Figure 8 shows the thermoelectric transport properties of $Sn_{0.97}In_{0.015}Cd_{0.015}Te$-*x*%CdS samples as a function of temperature. As can be seen from Figure 8a, the electrical conductivities decrease with increasing amounts of CdS over the entire temperature range. Specifically, the room-temperature electrical conductivity decreases steadily from ~1541 S/cm for $Sn_{0.97}In_{0.015}Cd_{0.015}Te$ to ~988 S/cm for the sample with 5% CdS. The Seebeck coefficients, however, show negligible change with the CdS content, Figure 8b. Due to the declined electrical conductivities upon CdS nanostructuring, the power factors are also decreased with increasing *x*, Figure 8c. Specifically, the maximum power factor drops systematically from ~24.5 μW cm^{-1} K^{-2} in the

DOI: 10.1021/jacs.5b00837
J. Am. Chem. Soc. 2015, 137, 5100–5112

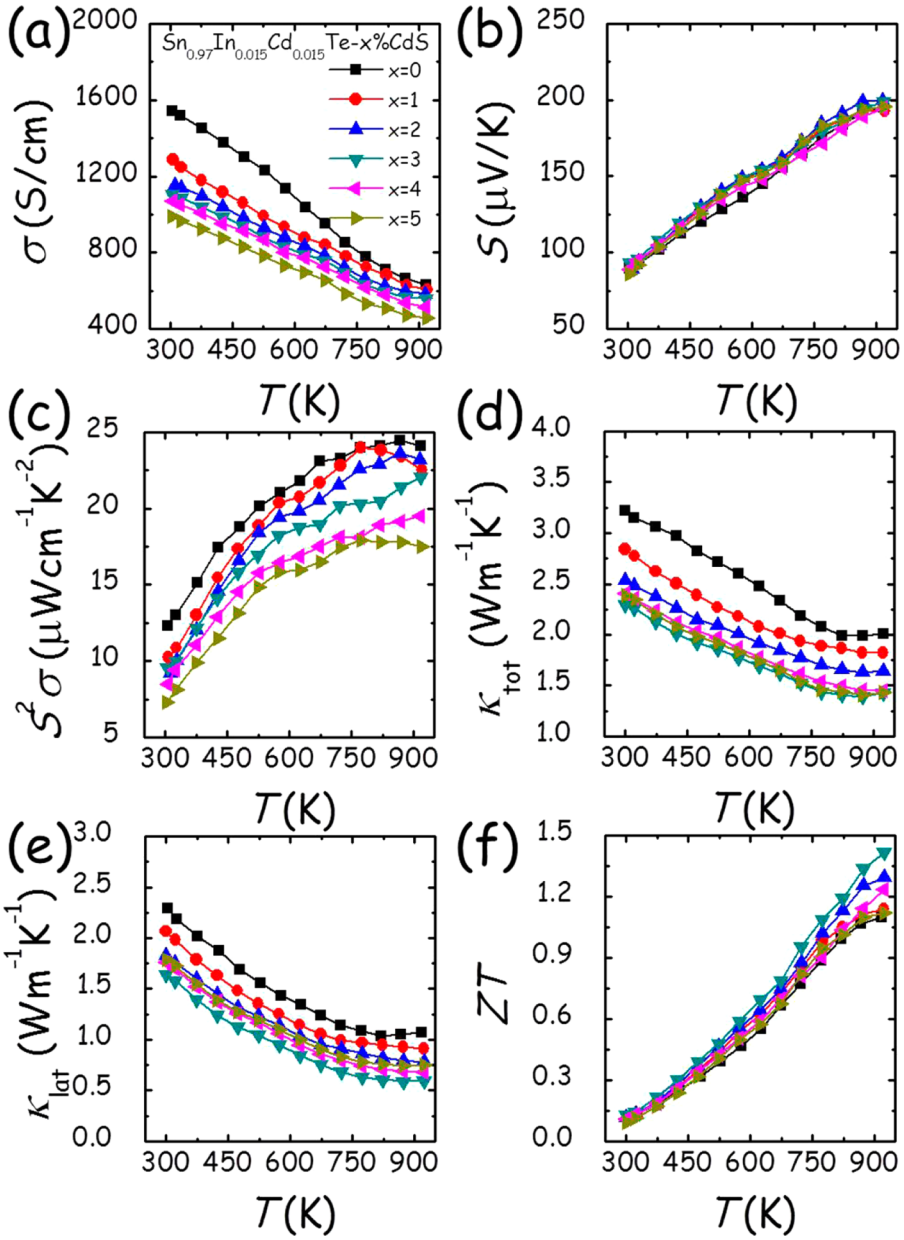

Figure 8. Thermoelectric transport properties as a function of temperature for $Sn_{0.97}In_{0.015}Cd_{0.015}Te$-$x$%CdS: (a) electrical conductivities; (b) Seebeck coefficients; (c) power factors; (d) total and (e) lattice thermal conductivities; and (f) ZT values.

control sample to ~17.9 μW cm^{-1} K^{-2} in the sample with x = 5.

The Hall measurements clarify the variations of electrical properties. Figure 9a plots room-temperature carrier concentrations (N_p) as a function of x for $Sn_{0.97}In_{0.015}Cd_{0.015}Te$-$x$% CdS. N_p are positive for all samples as expected. There is a slight decrease of N_p in the 1% CdS sample in comparison with the control sample $Sn_{0.97}In_{0.015}Cd_{0.015}Te$, probably due to their different cooling rates in the solidification process (see Experimental Section) which results in different levels of tin vacancies that have a significant impact on the hole densities. However, no apparent change of N_p is observed among samples with x from 1 to 5. This is reasonable because CdS has little solubility in SnTe (supported by the microscopy observations to be discussed in detail later). The carrier mobility μ_H shows a declining trend with increasing x which is attributed to the increased interfacial scattering by the CdS nanoprecipitates and accounts for the deterioration of electrical conductivities described above, Figure 9c.

The total (κ_{tot}) and lattice thermal conductivities (κ_{lat}) as a function of temperature for $Sn_{0.97}In_{0.015}Cd_{0.015}Te$-$x$%CdS are shown in Figure 8d,e, respectively, both of which show negative change with increasing amounts of CdS second phase. The lowest κ_{lat} of ~0.6 Wm^{-1} K^{-1} is obtained in the x = 3 sample at ~923 K, which is very close to the κ_{min} (~0.5 Wm^{-1} K^{-1}) of SnTe.[36,55] The reduction in lattice thermal conductivity seen in $Sn_{0.97}In_{0.015}Cd_{0.015}Te$-$x$%CdS is believed to arise from the well-dispersed CdS nanoprecipitates, which when combined with atomic-scale lattice distortions (doping) and mesoscale grains (by SPS) enable all-scaled length phonon scattering.[22,26]

Benefiting from the great reduction of lattice thermal conductivity, the ZTs are considerably enhanced upon CdS nanostructuring, with the highest value reaching ~1.4 at ~923 K for $Sn_{0.97}In_{0.015}Cd_{0.015}Te$ nanostructured with 3% CdS. This

DOI: 10.1021/jacs.5b00837
J. Am. Chem. Soc. 2015, 137, 5100−5112

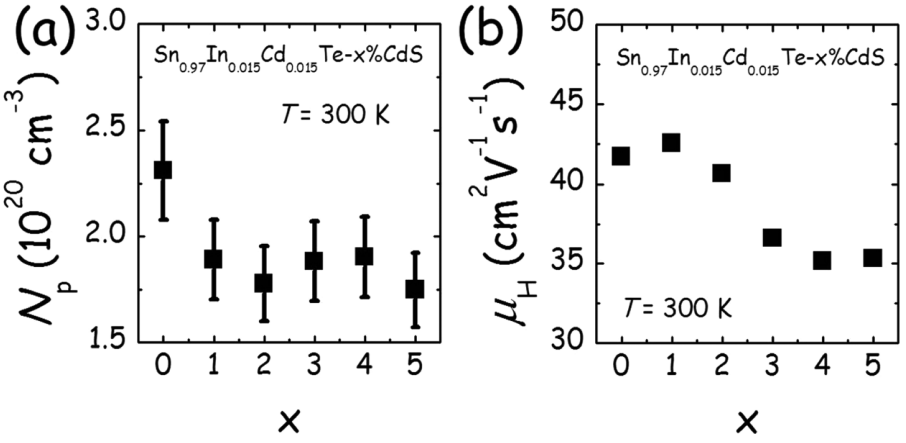

Figure 9. Room-temperature (a) carrier concentrations (N_p) and (b) mobilities (μ_H) as a function of second phase CdS amount (x) for $Sn_{0.97}In_{0.015}Cd_{0.015}Te$-$x$%CdS.

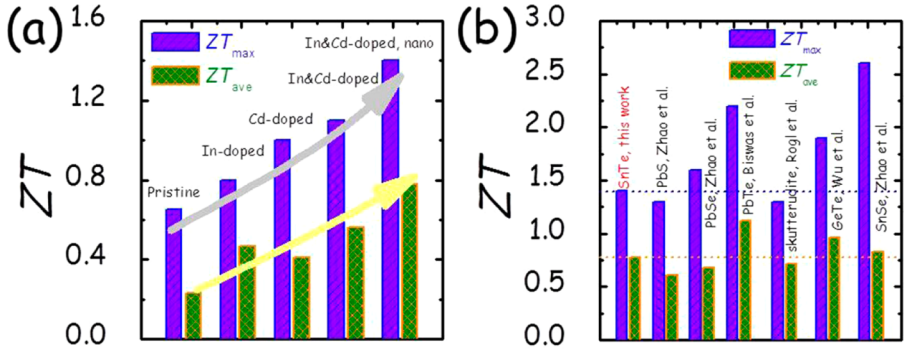

Figure 10. (a) Maximum (ZT_{max}) and average ZT (ZT_{ave}) for pristine SnTe, In- and Cd-doped SnTe, In and Cd codoped SnTe, and In and Cd codoped SnTe nanostructured with CdS. (b) Comparison of ZT_{max} and ZT_{ave} between optimized SnTe in the present study and leading p-type lead chalcogenides (PbS,[24] PbSe,[25] and PbTe[26]) as well as some other lead-free p-type systems (skutterudite,[59] GeTe,[60] and SnSe[38]).

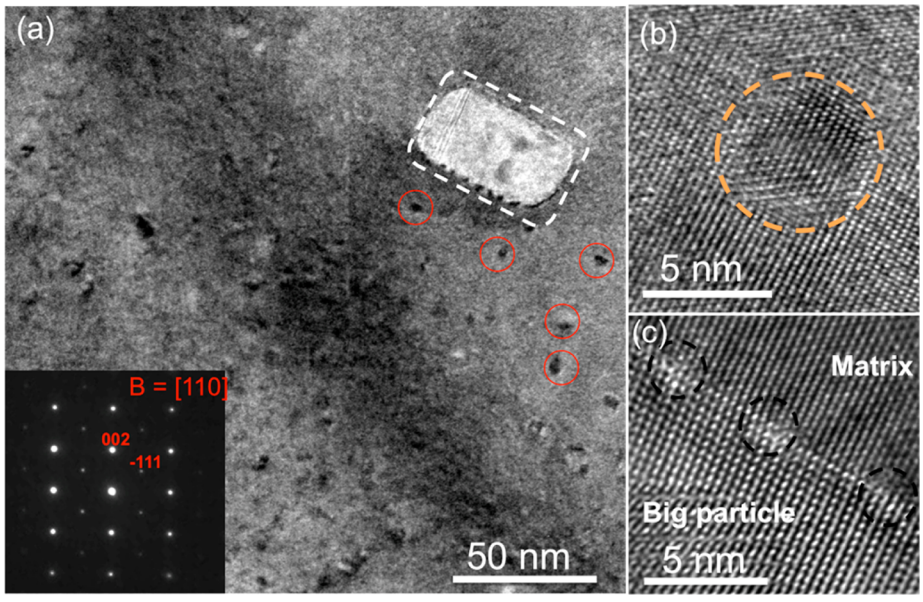

Figure 11. Electron microscopy of specimen $Sn_{0.97}In_{0.015}Cd_{0.015}Te$-3%CdS. (a) Low-magnification image of the specimen along [110] zone axis shows both small precipitate (red circles) and large precipitate (dashed white rectangular) in the matrix. The inset shows the corresponding SAD pattern. (b) A HRTEM image of one of the small precipitates, highlighted by the dashed orange circle, showing coherent interfaces between the matrix and the precipitate. (c) A HRTEM image of the interfaces between the big precipitate and the matrix. Misfit dislocations are highlighted by the dashed black circles.

DOI: 10.1021/jacs.5b00837
J. Am. Chem. Soc. 2015, 137, 5100−5112

value is the best result reported so far for p-type SnTe and is a ~115% improvement over the pristine SnTe and a ~27% improvement over the control sample $Sn_{0.97}In_{0.015}Cd_{0.015}Te$. More importantly, beyond ZT_{max}, the average ZT of ~0.78 between 300 and 923 K is among the largest achieved so far in the SnTe systems. More importantly, the thermoelectric properties of this high-performing sample showed negligible change in the heating−cooling thermal cycles (Figure S6) we used, demonstrating its good stability which was the major concern in nanostructuring materials. Long-term studies however were not performed.

Figure 10a schematically summarizes the stage by stage processes that lead to high performance in SnTe. Utilizing the concepts of resonant levels and band convergence to modify the electronic structure of SnTe individually, one can readily improve both ZT_{max} and ZT_{ave} relative to pristine SnTe. Combining the two approaches yields even larger ZT_{max} and ZT_{ave} due to the broadening enhancement of Seebeck coefficients. Finally, applying the all-scale hierarchical microstructuring approach to scatter a wide spectrum of phonons, a record high ZT_{max} of ~1.4 at ~923 K and a largely enhanced ZT_{ave} of ~0.78 between 300 and 923 K are achieved.

Figure 10b compares the maximum and average ZTs between SnTe in this work and the well-developed p-type lead chalcogenides[24−26] along with some other p-type lead-free thermoelectrics (skutterudite,[59] GeTe,[60] and SnSe[38]) from available literatures. Compared to other p-type systems, SnTe has a good enough ZT_{max} and an outstanding ZT_{ave}. Along with the advantage of Pb-free composition (although Cd is regarded as toxic element also, its low content here makes it inconsequential) and apparent good thermal stability, SnTe holds great promise as a substitute of lead chalcogenides for high-temperature thermoelectric power generation.

Scanning and Scanning Transmission Electron Microscopy (S/TEM). The microstructures and chemical compositions of the $Sn_{0.97}In_{0.015}Cd_{0.015}Te$-3%CdS specimen were investigated by TEM and STEM EDS, respectively. Figure 11a shows a low-magnification image of the nanoscale precipitates in the In and Cd codoped SnTe matrix along [110] orientation. Both small precipitates (red circles) and large particles (dashed white rectangular) are observed in the matrix, but only one set of Bragg diffraction spots are shown in the inset selected area diffraction (SAD) pattern of the corresponding area, taken with an aperture that captures both the matrix and the precipitates. This suggests that (i) no distinguishable difference exists between the matrix and the small precipitate lattice spacings, owing to their small lattice mismatch; (ii) the precipitates and the matrix have the same orientation (endotaxy); and (iii) the density of the large particles is considerably lower than the small ones, thus the difference cannot be observed in the SAD pattern.

HRTEM images of the small and larger precipitates are shown in Figure 11b,c, respectively. Figure 11b shows a 5 nm precipitate embedded in the matrix with coherent interfaces, highlighted by the dashed orange circle. Misfit dislocations were highlighted by the dashed black circles at the interfaces of big particles and the matrix, which reveal semicoherent interfaces. Such interfaces can also scatter phonons as well as electrons, which affect the thermoelectric properties, Figures 8e and 9b.

Chemical compositions of the precipitates were confirmed by STEM EDS as shown in Figure 12. A line scan was performed on the big particle as shown in the inset of STEM image. Cd and S peaks are clearly resolved in the big precipitate, but very

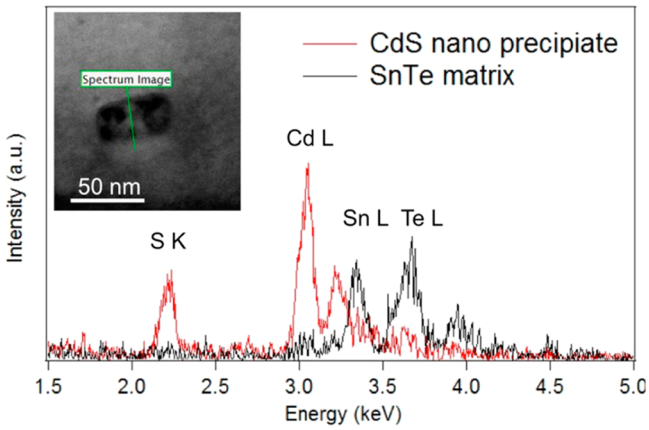

Figure 12. STEM EDS on the big precipitate shown in Figure 11a. Cd and S are found in the precipitate. The Cd and S (very little) found in the matrix might form solid solution with the matrix.

few traces corresponding to S were found in the matrix. The Cd L peak found in the matrix is the evidence that Cd is codoped in the SnTe matrix, but indium is difficult to resolve because the In L peaks overlap with the Sn L and Te L peaks. Nanostructuring with CdS in the In/Cd codoped SnTe, coupled with lattice distortions by elemental substitution as well as mesoscale grains forms an all-scale hierarchical system that can effectively scatter phonons,[26,61] resulting in very low lattice thermal conductivity and high figure of merit ZT as shown in Figure 8f.

CONCLUDING REMARKS

The coexistence of resonant levels (by In dopant) and band convergence (by Cd dopant) in a single material has been shown to act synergistically to produce a large improvement in the Seebeck coefficient of SnTe over a very broad temperature range. We find that codoping of In and Cd has a cumulative beneficial effect on the overall performance without any apparent interference of counter-indicated behavior of the two dopants. In addition, the atomic-scale lattice distortions (In and Cd codoping), nanoscale nanoprecipitates (CdS), and mesoscale grains (introduced by SPS treatment) form all-scale hierarchical microstructuring in the material that efficiently scatters a wide spectrum of heat-carrying phonons, leading to significantly reduced lattice thermal conductivity. As a consequence, the highest ZT of ~1.4 at ~923 K was achieved in the SnTe system by In and Cd codoping and with hierarchical structuring. In addition, the average ZT of this system improves considerably from 0.23 to ~0.78 between 300 and 900 K, making this material system a promising lead-free thermoelectric and a viable candidate for high-temperature power generation studies if lead-free materials must be used.

ASSOCIATED CONTENT

Supporting Information

Room-temperature densities (Table S1), powder XRD patterns (Figure S1), temperature-dependent heat capacities (Figure S2), thermal diffusivities (Figure S3), and Lorenz numbers (Figure S5) for all the samples investigated in this study. Detailed DFT band structures of nondoped, In- and Cd-doped and In/Cd codoped SnTe (Figure S4). Thermal stability of $Sn_{0.97}In_{0.015}Cd_{0.015}Te$-3%CdS as assessed by the unchanged thermoelectric properties in the heating−cooling thermal cycles

DOI: 10.1021/jacs.5b00837
J. Am. Chem. Soc. 2015, 137, 5100−5112

(Figure S6). This material is available free of charge via the Internet at http://pubs.acs.org.

AUTHOR INFORMATION

Corresponding Author

*m-kanatzidis@northwestern.edu

Notes

The authors declare no competing financial interest.

ACKNOWLEDGMENTS

This work was supported as part of the Revolutionary Materials for Solid State Energy Conversion, an Energy Frontier Research Center funded by the U.S. Department of Energy, Office of Science, and Office of Basic Energy Sciences under award number DE-SC0001054. Transmission electron microscopy work was partially performed in the EPIC facility of the NUANCE Center at Northwestern University. Access to facilities of high-performance computational resources at the Northwestern University is acknowledged.

REFERENCES

(1) Rowe, D. M. *CRC handbook of thermoelectrics*; CRC Press: Boca Raton, FL, 1995.
(2) Rowe, D. M. *Thermoelectrics handbook: macro to nano*; CRC Press: Boca Raton, FL, 2005.
(3) Bell, L. E. *Science* **2008**, *321*, 1457.
(4) Hsiao, Y.; Chang, W.; Chen, S. *Energy* **2010**, *35*, 1447.
(5) Yu, C.; Chau, K. *Energy Convers. Manage.* **2009**, *50*, 1506.
(6) Ravich, Y. I.; Efimova, B.; Smirnov, I. In *Semiconducting Lead Chalcogenides*; Springer Science: New York, 1970; p 323.
(7) Khokhlov, D. *Lead chalcogenides: physics and applications*; CRC Press: Boca Raton, FL, 2002.
(8) He, J.; Kanatzidis, M. G.; Dravid, V. P. *Mater. Today* **2013**, *16*, 166.
(9) Zhao, L.-D.; Dravid, V. P.; Kanatzidis, M. G. *Energy Environ. Sci.* **2014**, *7*, 251.
(10) Kanatzidis, M. G. *Chem. Mater.* **2009**, *22*, 648.
(11) Pei, Y.; Wang, H.; Snyder, G. *Adv. Mater.* **2012**, *24*, 6125.
(12) LaLonde, A. D.; Pei, Y.; Wang, H.; Jeffrey Snyder, G. *Mater. Today* **2011**, *14*, 526.
(13) Heremans, J. P.; Jovovic, V.; Toberer, E. S.; Saramat, A.; Kurosaki, K.; Charoenphakdee, A.; Yamanaka, S.; Snyder, G. J. *Science* **2008**, *321*, 554.
(14) Heremans, J. P.; Wiendlocha, B.; Chamoire, A. M. *Energy Environ. Sci.* **2012**, *5*, 5510.
(15) Ahn, K.; Han, M.-K.; He, J.; Androulakis, J.; Ballikaya, S.; Uher, C.; Dravid, V. P.; Kanatzidis, M. G. *J. Am. Chem. Soc.* **2010**, *132*, 5227.
(16) Wang, S.; Tan, X.; Tan, G.; She, X.; Liu, W.; Li, H.; Liu, H.; Tang, X. *J. Mater. Chem.* **2012**, *22*, 13977.
(17) Zhang, Q.; Liao, B.; Lan, Y.; Lukas, K.; Liu, W.; Esfarjani, K.; Opeil, C.; Broido, D.; Chen, G.; Ren, Z. *Proc. Natl. Acad. Sci. U.S.A.* **2013**, *110*, 13261.
(18) Pei, Y.; Shi, X.; LaLonde, A.; Wang, H.; Chen, L.; Snyder, G. J. *Nature* **2011**, *473*, 66.
(19) Liu, W.; Tan, X.; Yin, K.; Liu, H.; Tang, X.; Shi, J.; Zhang, Q.; Uher, C. *Phys. Rev. Lett.* **2012**, *108*, 166601.
(20) Zhang, Q.; Cao, F.; Liu, W.; Lukas, K.; Yu, B.; Chen, S.; Opeil, C.; Broido, D.; Chen, G.; Ren, Z. *J. Am. Chem. Soc.* **2012**, *134*, 10031.
(21) Pei, Y.; LaLonde, A. D.; Heinz, N. A.; Snyder, G. J. *Adv. Energy Mater.* **2012**, *2*, 670.
(22) Zhao, L.; Wu, H.; Hao, S.; Wu, C.; Zhou, X.; Biswas, K.; He, J.; Hogan, T.; Uher, C.; Wolverton, C. *Energy Environ. Sci.* **2013**, *6*, 3346.
(23) Biswas, K.; He, J.; Zhang, Q.; Wang, G.; Uher, C.; Dravid, V. P.; Kanatzidis, M. G. *Nat. Chem.* **2011**, *3*, 160.
(24) Zhao, L.-D.; He, J.; Hao, S.; Wu, C.-I.; Hogan, T. P.; Wolverton, C.; Dravid, V. P.; Kanatzidis, M. G. *J. Am. Chem. Soc.* **2012**, *134*, 16327.
(25) (a) Zhao, L.-D.; Hao, S.; Lo, S.-H.; Wu, C.-I.; Zhou, X.; Lee, Y.; Li, H.; Biswas, K.; Hogan, T. P.; Uher, C. *J. Am. Chem. Soc.* **2013**, *135*, 7364. (b) He, J. Q.; Girard, S. N.; Kanatzidis, M. G.; Dravid, V. P. *Advanced Functional Materials* **2010**, *20*, 764−772.
(26) (a) Biswas, K.; He, J.; Blum, I. D.; Wu, C.-I.; Hogan, T. P.; Seidman, D. N.; Dravid, V. P.; Kanatzidis, M. G. *Nature* **2012**, *489*, 414. (b) Androulakis, J.; Lin, C.-H.; Kong, H.-J.; Uher, C.; Wu, C.-I.; Hogan, T.; Cook, B. A.; Caillat, T.; Paraskevopoulos, K. M.; Kanatzidis, M. G. *J. Am. Chem. Soc.* **2007**, *129*, 9780−9788. (c) Cook, B. A.; Kramer, M. J.; Harringa, J. L.; Han, M. K.; Chung, D. Y.; Kanatzidis, M. G. *Advanced Functional Materials* **2009**, *19*, 1254−1259. (d) Levin, E. M.; Cook, B. A.; Ahn, K.; Kanatzidis, M. G.; Schmidt-Rohr, K. *Phys. Rev. B* **2009**, *80*, 115211-1−115211-6.
(27) Lee, Y.; Lo, S.-H.; Androulakis, J.; Wu, C.-I.; Zhao, L.-D.; Chung, D.-Y.; Hogan, T. P.; Dravid, V. P.; Kanatzidis, M. G. *J. Am. Chem. Soc.* **2013**, *135*, 5152.
(28) He, J.; Girard, S. N.; Zheng, J. C.; Zhao, L.; Kanatzidis, M. G.; Dravid, V. P. *Adv. Mater.* **2012**, *24*, 4440.
(29) Girard, S. N.; He, J.; Zhou, X.; Shoemaker, D.; Jaworski, C. M.; Uher, C.; Dravid, V. P.; Heremans, J. P.; Kanatzidis, M. G. *J. Am. Chem. Soc.* **2011**, *133*, 16588.
(30) Johnsen, S.; He, J.; Androulakis, J.; Dravid, V. P.; Todorov, I.; Chung, D. Y.; Kanatzidis, M. G. *J. Am. Chem. Soc.* **2011**, *133*, 3460.
(31) Hsu, K. F.; Loo, S.; Guo, F.; Chen, W.; Dyck, J. S.; Uher, C.; Hogan, T.; Polychroniadis, E.; Kanatzidis, M. G. *Science* **2004**, *303*, 818.
(32) Tan, G.; Zhao, L.-D.; Shi, F.; Doak, J. W.; Lo, S.-H.; Sun, H.; Wolverton, C.; Dravid, V. P.; Uher, C.; Kanatzidis, M. G. *J. Am. Chem. Soc.* **2014**, *136*, 7006.
(33) Zhou, M.; Gibbs, Z. M.; Wang, H.; Han, Y.; Xin, C.; Li, L.; Snyder, G. J. *Phys. Chem. Chem. Phys.* **2014**, *16*, 20741.
(34) Shi, F.; Lo, S.-H.; Tan, G.; Zhao, L.-D.; Kanatzidis, M. G.; Dravid, V. *Microsc. Microanal.* **2014**, *20*, 438.
(35) Banik, A.; Biswas, K. *J. Mater. Chem. A* **2014**, *2*, 9620.
(36) Tan, G.; Shi, F.; Doak, J. W.; Sun, H.; Zhao, L.-D.; Wang, P.; Uher, C.; Wolverton, C.; Dravid, V. P.; Kanatzidis, M. G. *Energy Environ. Sci.* **2015**, *8*, 267.
(37) Banik, A.; Shenoy, U. S.; Anand, S.; Waghmare, U. V.; Biswas, K. *Chem. Mater.* **2015**, *27*, 581.
(38) Zhao, L.-D.; Lo, S.-H.; Zhang, Y.; Sun, H.; Tan, G.; Uher, C.; Wolverton, C.; Dravid, V. P.; Kanatzidis, M. G. *Nature* **2014**, *508*, 373.
(39) Brebrick, R.; Strauss, A. *Phys. Rev.* **1963**, *131*, 104.
(40) Rogers, L. *J. Phys. D: Appl. Phys.* **1968**, *1*, 845.
(41) Allgaier, R. *J. Appl. Phys.* **1961**, *32*, 2185.
(42) Sitter, H.; Lischka, K.; Heinrich, H. *Phys. Rev. B* **1977**, *16*, 680.
(43) Brebrick, R. *J. Phys. Chem. Solid.* **1963**, *24*, 27.
(44) Bushmarina, G.; Gruzinov, B.; Drabkin, I.; Lev, E. Y.; Yuneev, V. *Sov. Phys. Semicond.* **1984**, *18*, 1374.
(45) Kaidanov, V.; Nemov, S.; Ravich, Y. I. *Sov. Phys. Semicond.* **1992**, *26*, 113.
(46) Borup, K. A.; de Boor, J.; Wang, H.; Drymiotis, F.; Gascoin, F.; Shi, X.; Chen, L.; Fedorov, M. I.; Muller, E.; Iversen, B. B.; Snyder, G. J. *Energy Environ. Sci.* **2015**, *8*, 423.
(47) Perdew, J. P.; Burke, K.; Ernzerhof, M. *Phys. Rev. Lett.* **1996**, *77*, 3865.
(48) Kresse, G.; Furthmüller, J. *Phys. Rev. B* **1996**, *54*, 11169.
(49) Popescu, V.; Zunger, A. *Phys. Rev. B* **2012**, *85*, 085201.
(50) Popescu, V.; Zunger, A. *Phys. Rev. Lett.* **2010**, *104*, 236403.
(51) Nashchekina, O.; Rogacheva, E.; Popov, V. *J. Phys. Chem. Solid.* **2008**, *69*, 273.
(52) Rogacheva, E. *J. Phys. Chem. Solid.* **2008**, *69*, 259.
(53) Tan, G.; Liu, W.; Chi, H.; Su, X.; Wang, S.; Yan, Y.; Tang, X.; Wong-Ng, W.; Uher, C. *Acta Mater.* **2013**, *61*, 7693.
(54) Tan, G.; Wang, S.; Yan, Y.; Li, H.; Tang, X. *J. Alloys Compd.* **2012**, *513*, 328.

DOI: 10.1021/jacs.5b00837
J. Am. Chem. Soc. 2015, 137, 5100−5112

(55) Tan, G.; Shi, F.; Sun, H.; Zhao, L.-D.; Uher, C.; Dravid, V. P.; Kanatzidis, M. G. *J. Mater. Chem. A* **2014**, *2*, 20849.
(56) Cahill, D. G.; Watson, S. K.; Pohl, R. O. *Phys. Rev. B* **1992**, *46*, 6131.
(57) Girard, S. N.; He, J.; Li, C.; Moses, S.; Wang, G.; Uher, C.; Dravid, V. P.; Kanatzidis, M. G. *Nano Lett.* **2010**, *10*, 2825.
(58) He, J.; Girard, S. N.; Kanatzidis, M. G.; Dravid, V. P. *Adv. Funct. Mater.* **2010**, *20*, 764.
(59) Rogl, G.; Grytsiv, A.; Rogl, P.; Bauer, E.; Hochenhofer, M.; Anbalagan, R.; Mallik, R.; Schafler, E. *Acta Mater.* **2014**, *76*, 434.
(60) Wu, D.; Zhao, L.-D.; Hao, S.; Jiang, Q.; Zheng, F.; Doak, J. W.; Wu, H.; Chi, H.; Gelbstein, Y.; Uher, C.; Wolverton, C.; Kanatzidis, M. G.; He, J. *J. Am. Chem. Soc.* **2014**, *136*, 11412.
(61) Tan, G.; Zheng, Y.; Tang, X. *Appl. Phys. Lett.* **2013**, *103*, 183904.

DOI: 10.1021/jacs.5b00837
J. Am. Chem. Soc. 2015, 137, 5100−5112